PCCP

ROYAL SOCIETY OF CHEMISTRY

PAPER

Cite this: *Phys. Chem. Chem. Phys.*, 2023, **25**, 21456

The multiple physical quantity sensor based on cylindrical photonic crystals with XOR logic gates

Ding-Yuan Zhang,[a] Jun-Yang Sui,[b] You-Ming Liu[b] and Hai-Feng Zhang *[b]

Received 22nd May 2023,
Accepted 24th July 2023

DOI: 10.1039/d3cp02329j

rsc.li/pccp

Based on cylindrical photonic crystals in one dimension, a multi-scale sensor device with a logic operation is being proposed. At the same time, it can satisfy the functions of refractive index (RI) and magnetic field detection. Under the modulation of an external magnetic field, sharp absorption peaks (APs) are obtained in the terahertz (THz) range. In a certain frequency range (AP value above 0.9), as the particular InSb layers are applied to two different magnetic fields, APs of the same frequency can be implemented to operate as XOR logic gates. The results show that with a change in the detected physical quantity, the frequency point of the corresponding AP also moves. Therefore, by adjusting the position of the AP, the magnetic field and RI can be sensed, and the device shows relatively excellent performance of 6879.88 and 6943.65 in terms of quality factor. In addition, the optimal performance of sensitivity, detection limit, and corresponding figure of merit is $0.01264(2\pi c/d_0)$ T^{-1}, 2.25×10^{-4} T, 227.23 T^{-1}, and $-0.003779(2\pi c/d_0)$ RIU^{-1}, 7.69×10^{-3} RIU, 67.74 RIU^{-1}. In terms of overall sensors, the proposed device is highly innovative in structure and meets the requirements of multi-scale measurements.

1. Introduction

In terms of electromagnetic wave (EW) propagation, photonic crystals (PCs) are periodic structures made up of different materials that can efficiently manipulate and maintain the EW propagation characteristics of the structure.[1] As a new type of electromagnetic medium, PCs are available in three arrangements of one-dimensional (1D), two-dimensional, and three-dimensional structures,[2] and intensive theoretical and experimental research has been conducted on them.[3–5] In particular, the cylindrical PCs (CPCs)[6] with periodic cylindrical multilayer structures show a higher performance compared to planar PCs. Studies have shown that CPCs have broad prospects and have been widely studied. As with currently available materials and methods for CPCs, many active and passive devices[7] have been proposed, including sensors,[8–10] laser light sources, modulators, channel filters and all-optical switches. In addition, their main advantages are that they can generate a complete band gap, improve lateral propagation constraints, and increase optical extraction.[11] More importantly, PC optical fibers can be formed by combining CPCs with optical fibers, which are different from ordinary optical fibers and have structural diversity.[12] The PCs' fiber structure makes PC fiber optic sensors extremely sensitive to changes in the refractive index while remaining compact and robust.[13]

The columnar PC structure uses InSb, which can further increase the regulatory characteristics of the magnetic field, especially for the semiconductor[14,15] materials located in the terahertz (THz) range.[16,17] Because high electron mobility semiconductors have cyclotron frequencies, the frequency in Hz at which a charged particle gyrates around a magnetic field with field strength in Gauss, the performance of their gyroscopes is near the cyclone frequency under the application of a sufficiently weak magnetic field, and irreversible transmission can be achieved. Similarly, as proposed by Xia *et al.*, in the THz state, the Indium Antimonide (InSb) hole array can be directly excited under a vertical direct current magnetic field (Faraday configuration) to directly excite the dominant anomalous surface magnetic plasma resonance,[18] a kind of surface resonance, which means that magnetoplasmon polaritons can also exist provided the magnetic field is appropriately configured. According to Wan *et al.*, the quasi-periodic structure of InSb was used to study unidirectional absorbers with narrow band angle polarization-sensitive regions to generate absorption bands whose polarization separation and non-reciprocal ability could be adjusted by temperature and magnetic induction intensity.[19] Furthermore, magnetized InSb can form magneto-optical crystal structures.[20] Due to the unique characteristics of the magnetic field strength being able to be adjusted, the

[a] *School of Communications and Information Engineering, Nanjing University of Posts and Telecommunications, Nanjing, 210023, China*
[b] *College of Electronic and Optical Engineering and the College of Flexible Electronics (Future Technology), Nanjing University of Posts and Telecommunications, Nanjing, 210023, China. E-mail: hanlor@163.com, hanlor@njupt.edu.cn*

corresponding magneto-optical devices have great potential for research in this area.

Devices can be applied for logic operations, physical quantity detection, and optical calculations, which have been widely studied due to their practical applications in integrated circuits and modern electronics, and additionally, the optical logic gates with multi-physical quantity detection[21,22] have attracted considerable attention and research. In the field of multi-physical quantity detection, the linear optical effects have been used effectively to design optical logic gates, including interferometry,[23] semiconductor optical amplifiers,[24] Mach-Zender interferometers,[25] and nonlinear processes such as electro-optical effects.[26,27] Based on the strength of the PC fiber in polarization, a temperature-insensitive hydrogen sensor is designed by Yang *et al.*, which in the scope of 1–4% hydrogen concentration has S = 131 pm%.[28] Besides, a 1D superstructure defect mode based on silicon, analyte, and silica layers was proposed by Sovizi *et al.*,[29] as a method for refractive index (RI) sensors with perpendicular and 45 incidence angles with sensitivity (S) that has exceeded 450 and 600 nm RIU^{-1}. Zhao *et al.* proposed a PC cavity electric field sensor,[30] and the detection limit (DL) and S are both 7 nW per V m^{-1} and 0.143 V m^{-1}, respectively. This clearly shows that logic gates can perform a large number of logic functions, enabling many applications of logic gates in multi-physical quantity detection. The multiphysical quantity sensor developed by Liu *et al.* uses a high-birefringence PC fiber surface plasmonic resonance effect to detect RI and ultrahigh S temperatures.[31] They draw our attention to the multifunctional sensor and provide quite innovative ideas for the relative field research, which has considerable application prospects and research value. But unfortunately, most of the research in this field is only based on a 1D planar structure,[21,22] which can only be used as a single-function device without more flexible practicality, cannot meet the application of multiple scenarios, and only focuses on the improvement of efficiency. There are a number of limitations that can be applied to research in the related fields. Electromagnetic devices, which possess multi-scale and multi-functional superiority, are worthy of further study and have considerable potential.

In this article, CPCs that simultaneously achieve logical operation capabilities and sensing detection functions are deeply investigated. Specifically, by utilizing the structural characteristics of CPCs and introducing magnetized InSb as a defect layer, a sharp absorption peak is generated to realize XOR logic operations modulated by a magnetic field. In addition to the logic operation function, with the change of external magnetic field and refractive index of the dielectric layer, the normalized angular frequency corresponding to the absorption peak also moves, which has a good linear fitting relationship and realizes the detection of multi-physical quantities regulated by multiple logic gates. The high S and high-quality factor (Q) enable the detection of small changes in the magnetic field or RI through the position of the absorption peak. Furthermore, this article highlights the different scales of the detection range with S and great Q values, achieving accurate multiphysical measurements. We would like to point out that this paper is primarily concerned with theoretical research, and that experimental research is beyond the scope of this current study, which is expected to be presented in the future.

2. Design and discussion

2.1. Theoretical model

By combining the methods of planar PCs and non-magnetized CPCs, a transfer matrix equation for the CPCs is derived. As shown in Fig. 1, the CPCs' model diagram is proposed, composed of ordinary A, B, C, D, E, F, and G dielectrics for non-symmetrical arrangement, where the air is the inner and outer layers with RI of n_0 as well as corresponding radiuses of ρ_0 and ρ_f, and "FGF" is a filter structure. Besides, the magneto-optical medium InSb layers are introduced into the original structure as defects, and its entire structure is exposed to 270 K of air to adapt to the general situation. And different dielectrics are filled with different colors in the figure to represent the model clearly.

In this paper, a normalized thickness d_0 is used, which has a value of 10 μm. In addition, the angular frequency ω is normalized, and ω is expressed in units of $(2\pi c/d_0)$, which is equal to α. The thickness of ordinary dielectric A, B, C, D, E, F, and G is replaced by d_A, d_B, d_C, d_D, d_E, d_F, and d_G, respectively, and the parameter values of each other are $0.33d_0$, $0.4d_0$, $0.75d_0$, $0.69d_0$, $0.7d_0$, $0.25d_0$ and $0.38d_0$, respectively. The RI values belonging to ordinary dielectrics are n_A = 2.74, n_B = 2.64, n_C = 2.2, n_D = 2.16, n_E = 1.1, n_F = 3.3, and n_G = 3.25. As the effective dielectric constant and permeability expressions were derived by Leiwin *et al.* based on the Mie resonance theory, the required RI can be determined in a wide range of applications.[32] Considering that this technology has been applied in real life,[33] the permittivity that is set in this paper can also be applied in real life. The defect layer is composed of two different semiconductors, $InSb_1$ and $InSb_2$, the thickness of which is $d_1 = 0.09d_0$ and $d_2 = 0.062d_0$, respectively. A magnetic field external to InSb causes its dielectric to behave as an anisotropic tensor, and the RI of the dielectric changes as the strength of the magnetic field increases. Because the device has positive and negative scales, B_1 and B_2 are external magnetic fields applied perpendicularly to $InSb_1$ and $InSb_2$ from the positive direction along the z-axis. In Fig. 1, EWs are incident from inside the cylinder, and the arrow direction of the wave vector k indicates its direction of incidence, forming an angle in the $\rho o \Phi$-plane, and the incidence angle is expressed by θ.

It is important to note that our work is mainly focused on a theoretical model. As a result of the thin thickness of the InSb layers and the lack of external magnetic fields, the ordinary dielectrics in this model are not affected. For experimental applications, gradient magnetic field coils were designed by Xuan *et al.*[34] since the magnetic field area exerted on a particular InSb layer is relatively small, while other dielectric layers are not affected. As can be seen from the results presented in this paper, an electric current can be used to generate a spatial linear magnetic field that is in compliance with the

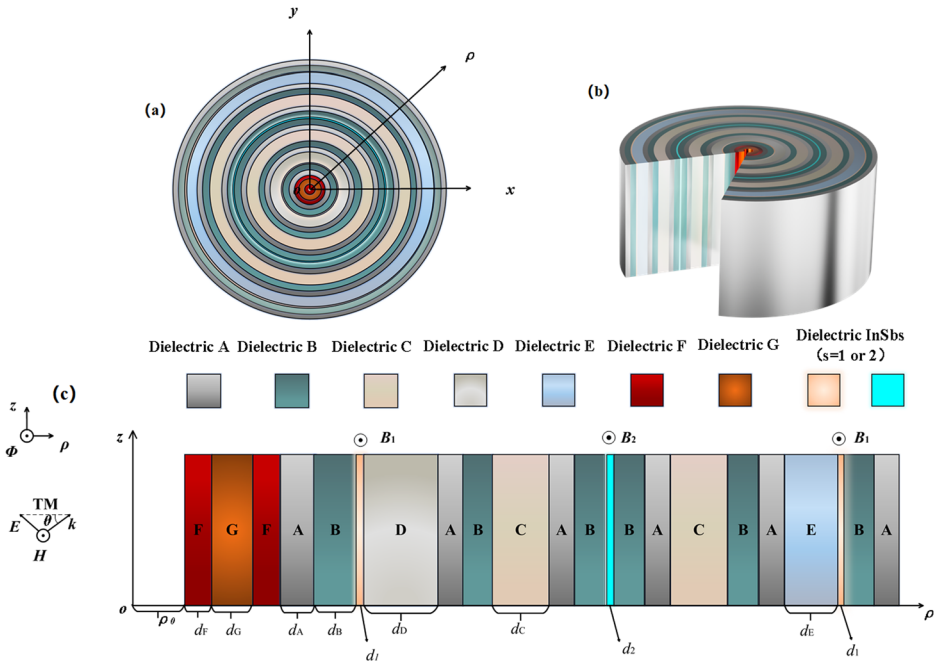

Fig. 1 The model diagrams of the CPC structure made up of different dielectric layers. (a) The view from the top of the model, (b) the front top view of the model, and (c) the cross-sectional view of the model along the radial angle in the ρoz-plane differentiation. As a reference, coordinate axes are used to mark the direction in which magnetic fields and EWs propagate.

requirements of this paper by isolating the influence of magnetic fields adjacent to different layers of InSb.

When EWs propagate in the CPCs, affected by Lorentz force, the external magnetic field mainly has a control function on transverse magnetic (TM) polarized EWs, while the transverse electronic (TE) polarization is not controlled by the magnetic field. TE waves refer to waves with an electric field perpendicular to the plane of transmission of light, while TM waves refer to waves with a magnetic field perpendicular to the plane of transmission of light. Therefore, this work will only focus on studying the performance of the CPC structure under TM polarization and analyze the entire structure by the transfer matrix method. After combining Maxwell's system of equations and the expression for the law of motion of charged particles, then the following form can be obtained:[35]

$$\frac{\mathrm{d}\mathbf{J}}{\mathrm{d}t} + v\mathbf{J} - \omega_\mathrm{c} \times \mathbf{J} = \varepsilon_0 {\omega_\mathrm{p}}^2 \mathbf{E}, \tag{1}$$

$$-\nabla \times \mathbf{E} = \mu_0 \frac{\partial \mathbf{H}}{\partial t}, \tag{2}$$

$$\nabla \times \mathbf{H} = \varepsilon_0 \frac{\partial \mathbf{E}}{\partial t} + \mathbf{J}, \tag{3}$$

where μ_0 and ε_0 represent respectively the permeability and the dielectric constant of air and $J = J_\rho + J_\varphi + J_z$ is the polarization current density:[35]

$$\begin{cases} (-jw + v)J_z = \varepsilon_0 {\omega_\mathrm{p}}^2 E_z \\ (-jw + v)J_\rho + J_\phi \omega_\mathrm{c} = \varepsilon_0 {\omega_\mathrm{p}}^2 E_\rho \\ (-jw + v)J_\phi - J_\rho \omega_\mathrm{c} = \varepsilon_0 {\omega_\mathrm{p}}^2 E_\phi \end{cases}, \tag{4}$$

$$\begin{pmatrix} J_\rho \\ J_\phi \\ J_z \end{pmatrix} = \varepsilon_0 \begin{pmatrix} \dfrac{{\omega_\mathrm{p}}^2 \omega_\mathrm{c}}{{\omega_\mathrm{c}}^2 - (\omega + jv)^2} & \dfrac{j{w_\mathrm{p}}^2(\omega + jv)}{(\omega + jv)^2 - {\omega_\mathrm{c}}^2} & 0 \\ \dfrac{j{w_\mathrm{p}}^2(\omega + jv)}{(\omega + jv)^2 - {\omega_\mathrm{c}}^2} & \dfrac{{\omega_\mathrm{p}}^2 \omega_\mathrm{c}}{-{\omega_\mathrm{c}}^2 + (\omega + jv)^2} & 0 \\ 0 & 0 & \dfrac{j{\omega_\mathrm{p}}^2}{\omega + jv} \end{pmatrix} \begin{pmatrix} E_\rho \\ E_\phi \\ E_z \end{pmatrix}. \tag{5}$$

The effective dielectric constant of InSb, an anisotropic material, can be obtained by applying an external magnetic field to the material and obtaining the following expression for the effective dielectric constant:[35]

$$\varepsilon_\mathrm{InSb} = \begin{bmatrix} \varepsilon_1 & j\varepsilon_2 & 0 \\ -j\varepsilon_2 & \varepsilon_1 & 0 \\ 0 & 0 & \varepsilon_3 \end{bmatrix}, \tag{6}$$

where

$$\varepsilon_1 = 1 - \frac{{\omega_\mathrm{p}}^2(\omega + j\nu_\mathrm{c})}{\omega\left[(\omega + j\nu_\mathrm{c})^2 - {\omega_\mathrm{c}}^2\right]}, \tag{7}$$

$$\varepsilon_2 = \frac{-{\omega_\mathrm{p}}^2 \omega_\mathrm{c}}{\omega\left[(\omega + j\nu_\mathrm{c})^2 - {\omega_\mathrm{c}}^2\right]}, \tag{8}$$

$$\varepsilon_3 = 1 - \frac{{\omega_\mathrm{p}}^2}{\omega(\omega + j\nu_\mathrm{c})}. \tag{9}$$

The plasma frequency is expressed as $\omega_p = (e^2 N_e/\varepsilon_0 m^*)^{1/2}$ and m^* represents the effective mass of the carrier, related to the mass of the electron m_e. And for InSb, $m^* = 0.015 m_e$. The cyclotron frequency of the electron is $\omega_c = eB_0/m^*$, which is proportional to the intensity of the applied electric field as can be seen, by the equation, the temperature T_0 has a great influence on it. Besides ω *is* expressed as the angular frequency of the incident waves. Moreover, the collision frequency, ν_c, is expressed separately in ν_{c1} and ν_{c2} for $InSb_1$ and $InSb_2$, as well as $\nu_{c1} = 6 \times 10^{-5}\omega_p$ and $\nu_{c2} = 8 \times 10^{-6}\omega_p$[16]. The magnetic strength is expressed by B_0, while electron quantity and quality are represented by e and m, respectively. The plasma density is expressed by N_e.

Therefore, eqn (3) can be derived as:[35]

$$\nabla \times H = \varepsilon_{ar}\varepsilon_{Insb}\frac{\partial E}{\partial t}. \tag{10}$$

Considering Maxwell's equations related to H polarization, the governing equations for E and H can be derived as:[35]

$$\frac{1}{\rho}\left[\frac{\partial(\rho E_\phi)}{\partial \rho} - \frac{\partial E_\rho}{\partial \phi}\right] = -j\omega\mu_0 H_z, \tag{11}$$

$$\frac{1}{\rho}\frac{\partial H_z}{\partial \phi} = j\omega\varepsilon_0\left(\varepsilon_1 E_\rho - j\varepsilon_2 E_\phi\right), \tag{12}$$

$$\frac{\partial H_z}{\partial \rho} = -j\omega\varepsilon_0\left(\varepsilon_1 E_\phi + j\varepsilon_2 E_\rho\right). \tag{13}$$

Then E_ρ and E_Φ are eliminated with H_z, and the following equation is derived:[35]

$$\begin{aligned}\frac{1}{\rho}\frac{1}{\omega\varepsilon_0(\varepsilon_1{}^2 - \varepsilon_2{}^2)}\Bigg\{&j\varepsilon_1\frac{\partial}{\partial\rho}\rho\frac{\partial H_z}{\partial\rho} - \varepsilon_2\frac{\partial}{\partial\rho}\frac{\partial H_z}{\partial\phi}\\ &\varepsilon_2\frac{\partial}{\partial\phi}\frac{\partial H_z}{\partial\rho} + j\varepsilon_1\frac{1}{\rho}\frac{\partial}{\partial\phi}\frac{\partial H_z}{\partial\phi}\Bigg\} = -j\omega\mu_0 H_z.\end{aligned} \tag{14}$$

The angle part meets the following conditions:[35]

$$\frac{d^2\Phi}{d\phi^2} + m^2\Phi = 0, \tag{15}$$

which has a solution $\Phi \sim e^{jm\varphi}$, and m can be set as an integer or a zero.

Combined with the standard Bessel's equation and eqn (14), magnetic and electric fields can be expressed as follows:[35]

$$H_z(\rho,\phi) = V(\rho)\Phi(\phi) = [AJ_m(k\rho) + BY_m(k\rho)]e^{j\omega\phi}, \tag{16}$$

where with azimuthal mode m, J_m and Y_m separately represent the Bessel and Neumann functions.

Then, substituting eqn (16) into eqn (12) and (13) yields the following two equations:

$$\frac{m}{\rho}V(\rho)e^{jm\varphi} = \omega\varepsilon_0\left(\varepsilon_1 E_\rho - j\varepsilon_2 E_\varphi\right), \tag{17}$$

$$\frac{\partial V}{\partial\rho}e^{j\omega\varphi} = -j\omega\varepsilon_0\left(\varepsilon_1 E_\varphi + j\varepsilon_2 E_\rho\right). \tag{18}$$

The following equation can be obtained:

$$\begin{aligned}E_\phi &= \left\{jp\left[AJ_m'(k\rho) + BY_m'(k\rho)\right]\right.\\ &\left. - \frac{jm\varepsilon_2}{\omega\varepsilon_0\rho(\varepsilon_1{}^2 - \varepsilon_2{}^2)}\left[AJ_m'(k\rho) + BY_m(k\rho)\right]\right\}e^{jm\phi}.\end{aligned} \tag{19}$$

The relevant expressions are then defined as:

$$E_\phi \equiv U(\rho)e^{im\phi}. \tag{20}$$

Besides, the form of $V(\rho)$ and $U(\rho)$ can respectively be calculated as follows:[35]

$$V(\rho) = AJ_m(k\rho) + BY_m(k\rho), \tag{21}$$

$$\begin{aligned}U(\rho) &= jp\left[AJ_m'(k\rho) + BY_m'(k\rho)\right]\\ &\quad - \frac{jm\varepsilon_2}{\omega\varepsilon_0\rho(\varepsilon_1{}^2 - \varepsilon_2{}^2)}[AJ_m(k\rho) + BY_m(k\rho)],\end{aligned} \tag{22}$$

where $p = (\mu/\varepsilon_0/\varepsilon_{Insb})^{1/2}\cos\theta$, $k = \omega p(\varepsilon_1{}^2 - \varepsilon_2{}^2)\varepsilon_0/\varepsilon_1$.

As for InSb, the refraction coefficient is $n_{TM} = \varepsilon_{TM}{}^{1/2}$, where the $\varepsilon_{TM} = (\varepsilon_1{}^2 - \varepsilon_2{}^2)/\varepsilon_1$.[4] Under TM polarization, the transfer matrix of InSb can be expressed in the following form, where $k = \omega n_{TM}\cos\theta/c$ is the component of the wave vector on the ρ-axis, $k_{iz} = \omega n_{TM}\cos\theta_i/c$ is a component of the wave vector in the z-axis, representing the wave vectors of $InSb_1$ or $InSb_2$, and $\eta_i = (\varepsilon_0/\mu_0)^{1/2}n_{TM}/\cos\theta_i$ is the light conductivity, where i is denoted by 1 or 2.

Thus, for different radii of the same dielectric, the following is a second-order transport matrix that represents the relationship between U and V:[35]

$$\begin{bmatrix}V(\rho_i)\\ U(\rho_i)\end{bmatrix} = \mathbf{M}_j\begin{bmatrix}V(\rho_{i-1})\\ U(\rho_{i-1})\end{bmatrix}, \tag{23}$$

where the A radius of $\rho_0 = 0.7$ μm is the core radius, and the radius of ρ_f is the outermost radius.

The $\mathbf{M}_j$ can be depicted as:[35]

$$\mathbf{M}_{TMi} = \begin{pmatrix}M_{11} & M_{12}\\ M_{21} & M_{22}\end{pmatrix}, \tag{24}$$

Then, according to $J_m(k\rho_0)Y_m'(k\rho_0) - J_m'(k\rho_0)Y_m(k\rho_0) = 2/(\pi k\rho)$,

$$\begin{aligned}M_{11} &= \left[-\frac{\pi m\varepsilon_2}{2\varepsilon_1}Y_m(k\rho_0) + \frac{\pi}{2}k\rho_0 Y_m'(k\rho_0)\right]J_m(k\rho)\\ &\quad + \left[\frac{\pi m\varepsilon_2}{2\varepsilon_1}J_m(k\rho_0) - \frac{\pi}{2}k\rho_0 J_m'(k\rho_0)\right]Y_m(k\rho)\end{aligned} \tag{25}$$

$$M_{12} = j\frac{\pi}{2}\frac{k}{p}\rho_0\cdot[Y_m(k\rho_0)J_m(k\rho) - J_m(k\rho_0)Y_m(k\rho)] \tag{26}$$

$$\begin{aligned} M_{21} &= \left[-\frac{\pi m\varepsilon_2}{2\varepsilon_1}Y_{\mathrm{m}}(k\rho_0)+\frac{\pi}{2}k\rho_0 Y_{\mathrm{m}}^{'}(k\rho_0)\right] \\ &\times\left[jpJ_{\mathrm{m}}^{'}(k\rho)-\frac{jm\varepsilon_2}{\omega\varepsilon_0\rho\left(\varepsilon_1{}^2-\varepsilon_2{}^2\right)}J_{\mathrm{m}}(k\rho)\right] \\ &+\left[\frac{\pi m\varepsilon_2}{2\varepsilon_1}J_{\mathrm{m}}(k\rho_0)-\frac{\pi k\rho_0}{2}J_{\mathrm{m}}^{'}(k\rho_0)\right] \\ &\times\left[jpY_{\mathrm{m}}^{'}(k\rho)-\frac{jm\varepsilon_2}{\omega\varepsilon_0\rho\left(\varepsilon_1{}^2-\varepsilon_2{}^2\right)}Y_{\mathrm{m}}(k\rho)\right] \end{aligned} \tag{27}$$

$$\begin{aligned} M_{22} &= -\frac{\pi}{2}k\rho_0\cdot Y_{\mathrm{m}}(k\rho_0)\left[J_{\mathrm{m}}^{'}(k\rho)-\frac{m\varepsilon_2}{\omega\varepsilon_0 p\rho\left(\varepsilon_1{}^2-\varepsilon_2{}^2\right)}\cdot J_{\mathrm{m}}(k\rho)\right] \\ &-\frac{\pi}{2}k\rho_0\cdot J_{\mathrm{m}}(k\rho_0)\left[Y_{\mathrm{m}}^{'}(k\rho)-\frac{m\varepsilon_2}{\omega\varepsilon_0 p\rho\left(\varepsilon_1{}^2-\varepsilon_2{}^2\right)}Y_{\mathrm{m}}(k\rho)\right] \end{aligned} \tag{28}$$

where $k_{\mathrm{TM}i}=\omega n_{\mathrm{TM}i}\cos\theta_{\mathrm{TM}i}/c$ is the component of the wave vector in the $\rho o\Phi$-plane, j can be indicated by A, B, C, D, E, F, and G, signified by different dielectric layer materials. Since the CPC structure is non-reciprocity, EWs propagate from the inside to the outside, corresponding to different transmission matrices, reflecting non-reciprocity. This article makes M the outgoing propagation transport matrix where the transfer matrices for dielectrics A, B, C, D, E, F, and G are represented by M_j, and $M_{\mathrm{TM}i}$ indicates the materials of $InSb_1$ and $InSb_2$.

Besides, as for the transfer matrix of the dielectrics, x indicates the name of the different materials, and i can be used to represent dielectrics layers A, B, C, D, E, F, and G. As ordinary dielectrics are unaffected by magnetic fields, their transfer matrix is indicated as:[35]

$$M_j=\begin{pmatrix} m_{11} & m_{12} \\ m_{21} & m_{22}\end{pmatrix}, \tag{29}$$

$$m_{11}=\frac{\pi}{2}k_i p_{i-1}\left[Y_{\mathrm{m}}^{'}(k_i\rho_{i-1})J_{\mathrm{m}}(k_i\rho_i)-J_{\mathrm{m}}^{'}(k_i\rho_{i-1})Y_{\mathrm{m}}(k_i\rho_i)\right], \tag{30}$$

$$m_{12}=-j\frac{\pi}{2}\frac{k_i}{p_i}\rho_{i-1}[J_{\mathrm{m}}(k_i\rho_{i-1})Y_{\mathrm{m}}(k_i\rho_i)-Y_{\mathrm{m}}(k_i\rho_{i-1})J_{\mathrm{m}}(k_i\rho_i)], \tag{31}$$

$$m_{21}=j\frac{\pi}{2}k_i p_i\rho_{i-1}\left[Y_{\mathrm{m}}^{'}(k_i\rho_{i-1})J_{\mathrm{m}}^{'}(k_i\rho_i)-J_{\mathrm{m}}^{'}(k_i\rho_{i-1})Y_{\mathrm{m}}^{'}(k_i\rho_i)\right], \tag{32}$$

$$m_{22}=\frac{\pi}{2}k_i\rho_{i-1}\left[J_{\mathrm{m}}(k_i\rho_{i-1})Y_{\mathrm{m}}^{'}(k_i\rho_i)-Y_{\mathrm{m}}(k_i\rho_{i-1})J_{\mathrm{m}}^{'}(k_i\rho_i)\right]. \tag{33}$$

Here is the complete positive transfer matrix **M**:[35]

$$\begin{aligned} M &= (M_G M_F M_G M_A M_B)M_{\mathrm{TM1}}(M_D M_A M_B M_C M_A M_B) \\ &\times M_{\mathrm{TM2}}(M_B M_A M_C M_B M_A M_E)M_{\mathrm{TM1}}(M_B M_A) \end{aligned} \tag{34}$$

$$\begin{aligned} M^{-1} &= \begin{pmatrix} M_{11} & M_{12} \\ M_{21} & M_{22}\end{pmatrix}^{-1}=\frac{1}{\det M}\begin{pmatrix} M_{22} & -M_{12} \\ -M_{21} & M_{11}\end{pmatrix} \\ &= \begin{pmatrix} M_{11}^{'} & M_{12}^{'} \\ M_{21}^{'} & M_{22}^{'}\end{pmatrix}, \end{aligned} \tag{35}$$

where the specific expressions for M are given derived from the transfer matrixes of dielectrics A, B, C, D, E, F, and G as shown in eqn (29)–(33). In addition, ''det'' represents the determinant of the matrix which appears in eqn (35). As TM waves travel through $InSb_1$ and $InSb_2$ materials, the transfer matrices are M_{TM1} and M_{TM2}, and their definite expressions are expressed as eqn (24)–(28).

The transmittance coefficient and reflection coefficient of the CPC structure must first be determined to calculate the absorptance (A), which is calculated as:[35]

$$r=\frac{\left(M_{21}^{'}-jp_0C_{m0}^{(2)}M_{11}^{''}\right)+jp_fC_{mf}^{(2)}\left(M_{22}^{'}-jp_0C_{m0}^{(2)}M_{12}^{'}\right)}{\left(jp_0C_{m0}^{(1)}M_{11}^{'}-M_{21}^{'}\right)+jp_fC_{mf}^{(2)}\left(jp_0C_{m0}^{(1)}M_{12}^{'}-M_{22}^{'}\right)}, \tag{36}$$

$$t=\frac{-4\varepsilon_{\mathrm{r}}{}^{-1}\sqrt{\frac{\mu_0}{\varepsilon_0}}}{\pi K\rho_0 H_m^{(2)}(k\rho_0)H_m^{(1)}(k\rho_0)\left[\left(jp_0C_{m0}^{(1)}M_{11}^{'}-M_{21}^{'}\right)-jp_fC_{mf}^{(2)}\left(jp_0C_{m0}^{(1)}M_{12}^{'}-M_{22}^{'}\right)\right]}. \tag{37}$$

Below are the values for reflectance and transmittance:[36,37]

$$R=|r^2|, \tag{38}$$

$$T=|t^2|. \tag{39}$$

Through A, we write:

$$A=1-R-T \tag{40}$$

2.2. Analysis and discussion

The absorption spectra of the XOR logic gate are shown in Fig. 2, with the two external magnetic fields B_1 and B_2 respectively applied to $InSb_1$ and $InSb_2$. When one magnetic field exists, it is denoted by a logic level (LL) ''1'', otherwise LL is ''0''. Similarly, when a sharp absorbance peak (AP) exists, it is denoted by a LL of ''1'', and *vice versa* as ''0''. For a more intuitive embodiment, ''In_1'' indicates the state of existence of B_1, ''In_2'' symbolizes the magnetic field B_2, and ''Out'' stands for the state of presence of AP. As can be seen from Fig. 2(a), under the condition that the applied magnetic field B_1 is present and B_2 is absent, A is obtained and much greater than 0.9, of which the value is 0.9704. And the frequency corresponding to AP is 0.3874α, Q = 6795.7, forming a sharp AP. The states are ''In_1 = 1'', ''In_2 = 0'', and ''Out = 1'', related to

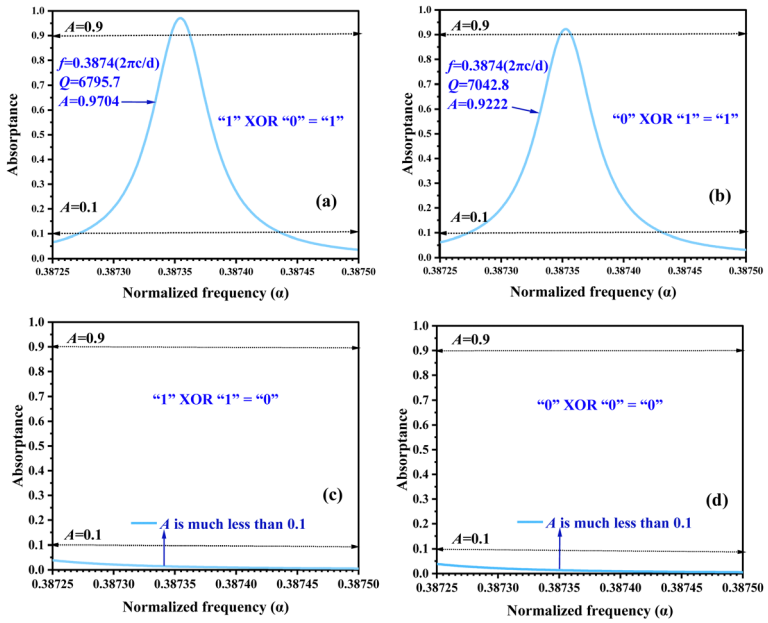

Fig. 2 Schematic diagrams of logic XOR operations controlled by magnetic fields and AP (>0.9) when EWs propagate.

Table 1 The XOR logic gate truth table (magnetic field presence and A value are indicated by "1" and "0")

In_1	In_2	Out
0	0	0 ($T < 0.1$)
1 (B_1 exists)	0	1 ($T > 0.9$)
0	1 (B_2 exists)	1 ($T > 0.9$)
1 (B_1 exists)	1 (B_2 exists)	0 ($T < 0.1$)

the "1 XOR 0 = 1" of the XOR logic gate. When B_1 does not exist and B_2 exists, A = 0.9222, much greater than 0.9, Q = 7042.8. The states are "In_1 = 0", "In_2 = 1", and "Out = 1" cohering with the "0 XOR 1 = 1" of the XOR logic gate. The AP of this case has the normalized angular frequency point (NAFP) of 0.3874 α, coinciding with "1 XOR 0 = 1", which is convenient for detecting logical operations.

When both B_1 and B_2 are subsistent, the AP does not exist, thatis is, "In_1 = 1", "In_2 = 1", and "Out = 0",. Aand A is much less than 0.1, correlating to the XOR logical operation "1 XOR 1 = 0". When neither B_1 nor B_2 is not existent, the AP is absent and A is much less than 0.1, then "In_1 = 0", "In_2 = 0", and "Out = 0" correspond to the "0 XOR 0 = 0" of the XOR logic gate. The absorbance spectra of the CPCs designed in our work strictly adhere to the XOR logic gate function from the inside to the outside of CPCs using external magnetic fields B_1 and B_2 to regulate. The logical truth table is shown in Table 1.

To better explain the causes of APs, we choose the best situation in which B_1 does not exist but B_2 exists (B_1 = 0 T and B_2 = 1.58 T) to explain the phenomenon. To observe the propagation of TM polarization waves more clearly in CPCs, as shown in Fig. 3, an electric field intensity distribution map with a normalized angular frequency ω of 0.3874α is produced, and thus illustrates the formation principle of AP. In the case of ω = 0.3874α, the surface partial electric field of the defect layer $InSb_2$ is enhanced, which stimulates the localization defect mode resonance, resulting in a sharp AP.

When there is a fixed external magnetic field, the magnetized InSb layers are still capable of detecting the other external magnetic field in the detection scope and are still able to perform XOR logic operations with good accuracy. This function can be maintained even with disparate linear ranges, and this is well worth emphasizing. Besides, the spatial distribution of A and the linear fitting relationship (LFR) can be obtained by the transport matrix method. Fig. 4 shows the $\rho o\Phi$-plane of the magnetic flux density B_1 detection. As depicted in Fig. 4(a), where B_1 varies and B_2 = 0 T, that is, the input LL is "In_1 = 1" and "In_2 = 0", AP changes under different NAFPs. However, when B_1 alters and B_2 is present constantly, its anteroposterior $\rho o\Phi$-plane view is shown in Fig. 4(b). It is obvious that no sharp AP exists and no linear range is formed that meets the requirements, which corresponds strictly to "1 XOR 1 = 0" in the XOR logic gate. Moreover, as the magnetic flux B_1 intensity increases, AP begins to show a continuous linear frequency shift and approximately keeps the bandwidth unchanged. As shown in Fig. 4(a), for magnetic field detection, continuous AP exhibits a good LFR and a stable bandwidth in the range of B_1 from 1.56 T to 1.66 T. And in this range, A is always greater than 0.9.

The good indicators for evaluating a sensor are S, Q, FOM, and DL. More importantly, high S, high Q, high FOM, and low DL reflect a good sensor. The corresponding definition follows, namely, Δf and Δn denote frequency and RI variations, respectively, f_T implies the frequency of AP, and the FWHM represents the width of the half-high resonant peak.[38]

$$S = \frac{\Delta f}{\Delta n}, \tag{41}$$

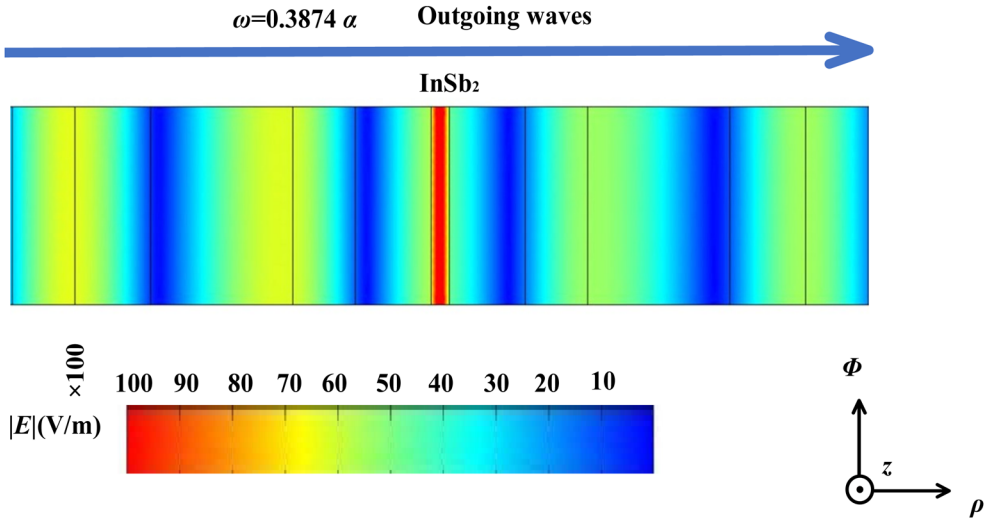

Fig. 3 The electric field distribution diagram at ω = 0.2645α when EWs propagate under the condition of B_1 = 0 T and B_2 = 1.58 T.

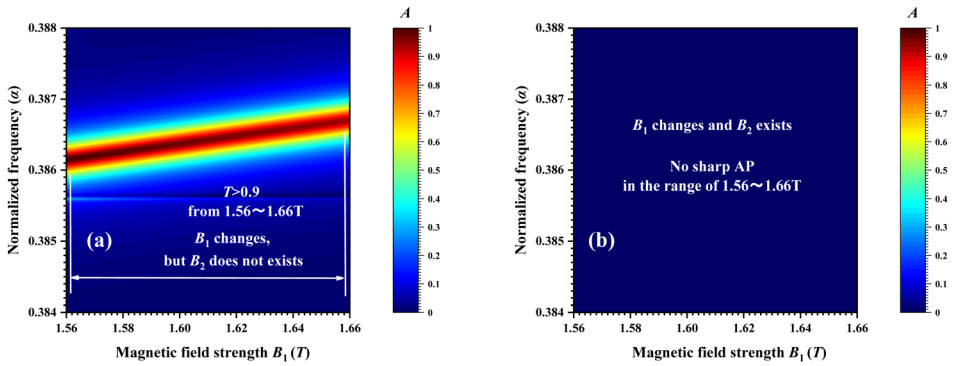

Fig. 4 The view from the top of AP varying with the NAFP and the magnetic field B_1: (a) the changes in the AP and the detection scope is 1.56–1.66 T when B_1 changes and B_2 does not. (b) The changes of AP and no sharp AP in 1.56–1.66 T when B_1 changes and B_2 exists.

$$\mathrm{FOM} = \frac{S}{\mathrm{FWHM}}, \tag{42}$$

$$Q = \frac{f_{\mathrm{T}}}{\mathrm{FWHM}}, \tag{43}$$

$$\mathrm{DL} = \frac{f_{\mathrm{T}}}{20SQ}. \tag{44}$$

To better analyze the magnetic field detection performance of CPCs, when B_1 changes and B_2 does not exist, the LFR between the related NAFP and the magnetic field strength B_1 is highlighted in Fig. 5(a). When B_1 is between 1.56 T and 1.66 T, the LFR is f = 0.01264B_1 + 0.3667, and 0.01264α/T is its S. The R^2 is 0.9999, which proves that the linearity is extraordinarily good and suitable for making sensors. Fig. 5 shows the Q and FOM values for detection, which are evaluative of the sensor, and the Q and FOM values generally decrease as the B_1 intensity increases. In addition, as shown in Fig. 5(b), after calculation, the average of Q, FOM, and DL are 6867.18, 224.08 T^{-1}, and 2.23×10^{-4} T respectively, which means that the performance parameters of the sensor still have a certain competitive advantage. As mentioned earlier, these sensing performance indicators can be made of a multi-scale magnetic field B_1 sensing detector. Furthermore, in the same measurement range, there are different Aps as well as different Q, FOM, and DL that can detect magnetic fields with different degrees of accuracy.

Under the condition that the external magnetic field B_1 = 0 T and B_2 is constantly changing, the CPCs proposed can still accurately detect the strength of B_2. First, an analysis of the positive scale is provided. Fig. 6 is the view from the top of AP, which illustrates intuitively the relationship between normalized target resonant peak frequency and B_2. The change in the magnetic field B_2 causes AP to drift, and when the EWs propagate outwards, B_2 varies in the range of 1.53 T to 1.63 T. The related A value is greater than 0.9, which meets the position AP requirement. The positive LFR of B_2 emerges in Fig. 7(a), the equation is f = 0.01261B_2 + 0.3666, and the 0.01261α/T is its S, indicating that the magnetic flux detection is extraordinarily sensitive. R^2 = 0.9997 symbolizes that it

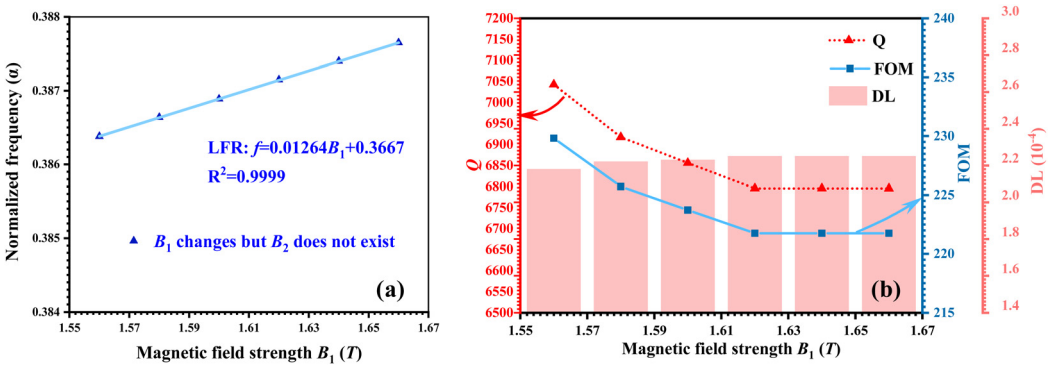

Fig. 5 (a) An analysis of the LFR between NAFP and the magnetic field strength B_1 when B_1 exists and B_2 does not. (b) The changes of Q, FOM and DL with B_1 varying under the conditions of "1 XOR 0 = 1", with 6867.18, 224.08 T^{-1} and 2.23 × 10^{-4} T as average values of Q, FOM and DL.

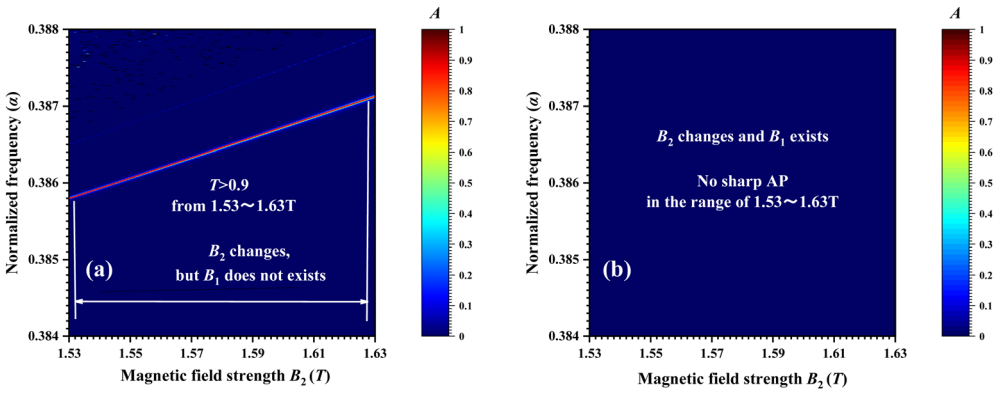

Fig. 6 The view from the top of AP varying with the NAFP and the magnetic field B_2: (a) the changes in the AP and the detection range is 1.53–1.63 T when B_1 does not and B_2 exists. (b) The changes in the AP and no sharp AP in 1.53–1.63 T when B_2 changes and B_1 exists.

exhibits excellent linearity over the detection range. As appeared in Fig. 7(b), 6979.88 and 227.23 T^{-1} severally correlate to the averages of Q and FOM. For this detection, the average DL is about 2.20 × 10^{-4} T, enabling more accurate magnetic flux density detection. In summary, the CPCs can perform accurate and wide-ranging magnetic field detection and can meet the XOR logic operation function.

In the chemical, biological, and medical fields, there is an urgent need for the identification of the RI of substances, so the sensors designed for RI detection are extraordinarily extensive.[39,40] The CPCs sensor is designed to not only realize magnetic field sensing detection but can also detect RI changes. To study the ability of CPCs to detect RI and the XOR logic operation function, when RI alters within a certain range, the medium n_E is set to the sensitive part, and the RI sensing function of CPCs is suitable for RI measurement of n_E. Fig. 8 indicates the $\rho o \Phi$-plane diagrams of the four logical cases in which XOR logic operates when EWs propagate positively. As shown in Fig. 8(a) and (b), when one of B_1 and B_2 exists and the other is not present, both the AP and its corresponding

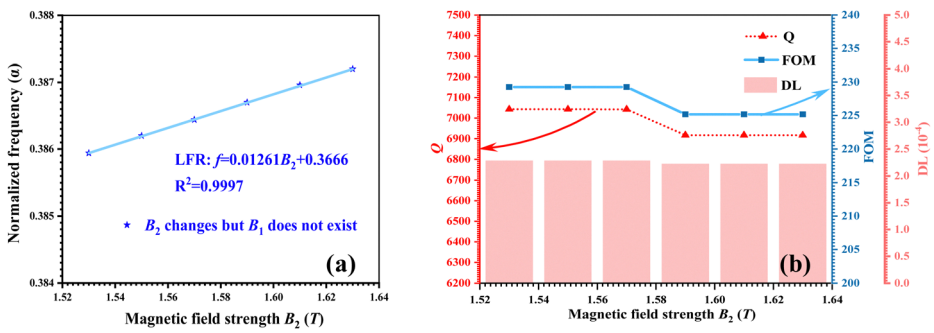

Fig. 7 (a) An analysis of LFR between NAFP and magnetic field strength B_2 when B_1 does not exist but B_2 does. (b) The changes of Q, FOM and DL with B_2 varying under the condition of "0 XOR 1 = 1", with 6979.88, 227.23 T^{-1} and 2.25 × 10^{-4} T as average values of Q, FOM and DL.

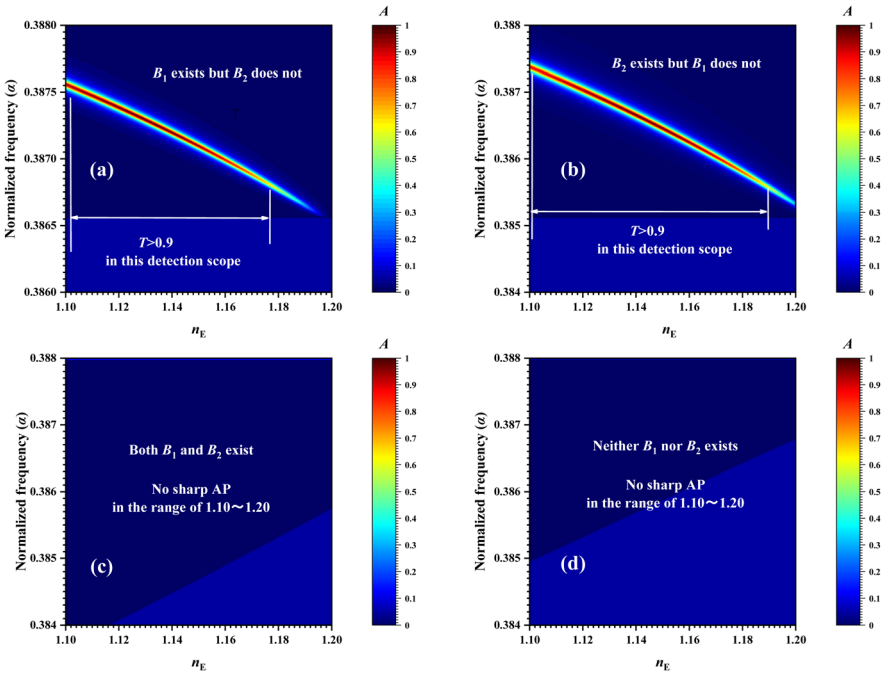

Fig. 8 The view from the top of AP varying with RI of n_E and the normalized frequency. (a) Changes in the AP when B_1 exists but B_2 does not when the detection range is 1.10–1.20. (b) Changes in the AP when B_2 exists but B_1 does not with the detection range of 1.10–1.20. (c) Changes in the AP when both B_1 and B_2 exist, and there is no sharp AP in 1.10–1.20. (d) Changes in the AP when neither B_1 nor B_2 exists, and no sharp AP in 1.10–1.20.

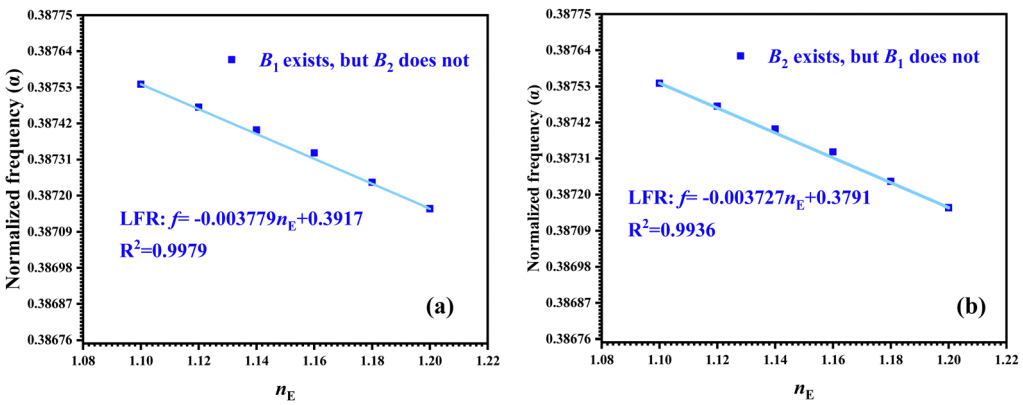

Fig. 9 LFR between NAFP and RI of n_E when "1 XOR 0 = 1" and "0 XOR 1 = 1".

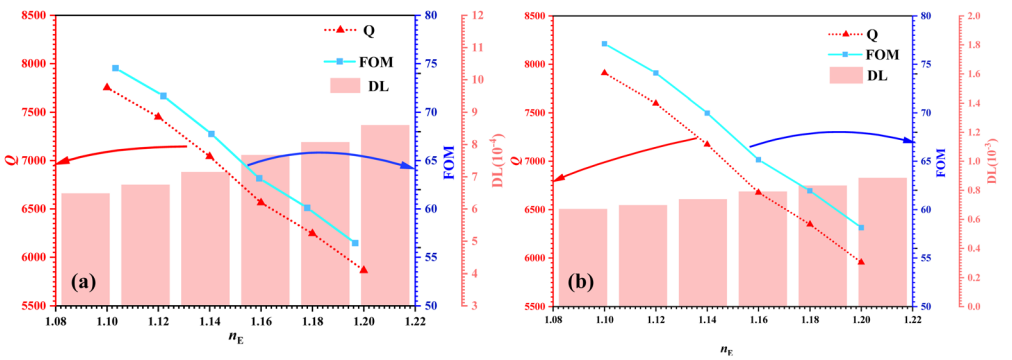

Fig. 10 The corresponding Q, FOM and DL with n_E varying. (a) The case of "1 XOR 0 = 1", with 6820.24, 67.74 RIU^{-1} and 7.45 × 10^{-3} RIU as the average values of Q, FOM and DL. (b) The case of "0 XOR 1 = 1", with 6943.65, 65.62 RIU^{-1} and 7.69 × 10^{-3} RIU as the average values of Q, FOM and DL.

Table 2 In comparison with published sensors, the proposed CPC sensors exhibit improved performance parameters

Ref.	Refractive index detection			Magnetic flux density detection			Logical operation
	Scope	S	Q	Scope	S	Q	
41	None			0.14–0.22T	2.67×10^{10} T^{-1}	—	None
42	1.3323–1.35612	677 nm RIU^{-1}	—	None			None
43	None			None			XOR and OR
44	1.362–1.366	303 376 nm RIU^{-1}	—	None			None
45	None			None			OR
46	1.4–1.4028	1.2×10^3 nm RIU^{-1}	1418.2	None			None
47	1.455–1.469	56.815 dBm RIU^{-1}	—	None			None
This work	1.1–1.2	$0.003779(2\pi c/d_0)$ RIU^{-1}	6879.88	1.53–1.66T	$0.01264(2\pi c/d_0)$ T^{-1}	6943.65	XOR

NAFP form a good LFR within their RI detection range, and they are A average values coinciding to 0.9634 and 0.9715 in several, which is much greater than 0.9, ensuring that the output LL is ''Out = 1''. When both B_1 and B_2 are existent or both are absent, as assumed in Fig. 8(c) and (d), no sharp AP appears. This means that the RI detection on the positive scale strictly follows the XOR logical operations ''1 XOR 0 = 1'', ''1 XOR 1 = 0'', ''0 XOR 1 = 1'' and ''0 XOR 0 = 0''.

It can be objectively seen from Fig. 9 that when the EWs are propagated outwards, the detection range of the RI of n_E is 1.10–1.20 under the conditions of maintaining B_1 = 1.62 T, B_2 = 0 T, and the corresponding LFR is $f = -0.003779n_E + 0.3917$, -0.003779α/RIU is S, and the R^2 of the equation is 0.9979, explaining excellent linearity. When B_1 = 0 T and B_2 = 1.58 T, the LFR correlating to n_E in the detection range of 1.10–1.20 is $f = -0.003727n_E + 0.3791$, $S = -0.003727\alpha$/RIU, and R^2 = 0.9936, which has good linearity.

The Q and FOM values related to the above two cases are demonstrated in Fig. 10 when input LL ''In_1 = 1'' and ''In_2 = 0''. After calculation, the average values of their corresponding Q, FOM, and DL are shown in Fig. 10(a), which are 6943.65, 65.62 RIU^{-1} and 7.38×10^{-4} RIU, separately. Fig. 10(b) shows a dotted line plot of Q and FOM values at ''In_1 = 0'' and ''In_2 = 1'', which shows that as n_E increases, both Q and FOM take on a rapid downward trend, belonging to the gradual decrease in sharpness of AP in Fig. 10(b). However, its Q, FOM, and DL averages are 6820.24, 67.74 RIU^{-1}, and 7.62×10^{-4} RIU, respectively, which can meet the sensing performance requirements. In the case of ''1 XOR 0 = 1'' and ''0 XOR 1 = 1'', the designed CPCs structure has good RI detection performance. In addition, compared with the case of ''In_1 = 1'' and ''In_2 = 0'', the situation of ''In_1 = 0'' and ''In_2 = 1'' has a similar DL and a larger FOM, and the device can meet relatively higher operating performance.

From the above research discussion, it can be concluded that the designed CPCs have performance values that can meet the requirements of magnetic field sensing and RI sensing. As shown in Table 2, the physical quantity sensing function designed in this work is based on the premise of the XOR logic operation function. From the input LL ''In_1'', ''In_2'' and the corresponding output LL ''Out'', it can be seen that it strictly follows the XOR logic operation function of ''1 XOR 0 = 1'', ''1 XOR 1 = 0'', ''0 XOR 1 = 1'' and ''0 XOR 0 = 0''. In addition, it also has a broader detection range and a variety of physical quantity detection functions at multiple scales, which both meet the regulation of logic gate functions.

3. Conclusion

A multi-scale sensor with a 1D CPC structure was proposed, which can integrate logic operation functions and multiple physical quantity detection functions. Using localized defect mode resonance, the structure achieves sharp AP ($A > 0.9$), and further adjusts the magnetic field to allow XOR logic operations with high Q values. In addition to this, our work achieves multi-physical quantity detection by varying the magnetic field strength and RI magnitude to lock the moving AP, which allows precise physical quantity sensing functions depending on its high S, R^2, FOM, and low DL. The sensing ranges corresponding to the magnetic field and RI are 1.53–1.63 T, 1.56–1.66 T, and 1.1–1.2, respectively. In conclusion, the proposed 1D CPC structure is highly novel in structure and has multi-scale and multi-functional detection, which is complementary to a single function and a single scale, and thus highly valuable for a theoretical study.

Conflicts of interest

There are no conflicts to declare.

Notes and references

1 G. Alagappan, X. W. Sun, P. Shum, M. B. Yu and M. T. Doan, One-dimensional anisotropic photonic crystal with a tunable bandgap, *J. Opt. Soc. Am. B*, 2006, **23**(1), 159–167.
2 M. A. Awad and A. H. Aly, Experimental and theoretical studies of hybrid multifunctional TiO_2/TiN/TiO_2, *Ceram. Int.*, 2019, **45**(15), 19036–19043.
3 B. Guo, Photonic band gap structures of obliquely incident electromagnetic wave propagation in a one-dimension absorptive plasma photonic crystal, *Phys. Plasmas*, 2009, **16**((4), 043508.
4 L. Qi, Z. Yang, F. Lan, X. Gao and Z. Shi, Properties of obliquely incident electromagnetic wave in one-dimensional magnetized plasma photonic crystals, *Phys. Plasmas*, 2010, **17**(4), 042501.

5 B. Guo, M. Q. Xie and L. Peng, Photonic band structures of one-dimensional photonic crystals doped with plasma, *Phys. Plasmas*, 2012, **19**(7), 072111.

6 J. Scheuer and A. Yariv, Annular Bragg defect mode resonators, *J. Opt. Soc. Am. B*, 2003, **20**(11), 2285–2291.

7 W. M. J. Green, J. Scheuer, G. DeRose and A. Yariv, Vertically emitting annular Bragg lasers using polymer epitaxial transfer, *Appl. Phys. Lett.*, 2004, **85**(17), 3669–3671.

8 M. M. Abadla, H. A. Elsayed and A. Mehaney, Sensitivity enhancement of annular one dimensional photonic crystals temperature sensors with nematic liquid crystals, *Phys. Scr.*, 2020, **95**(8), 085508.

9 M. M. Abadla, A. H. Elsayed and A. Mehaney, Thermo-optical properties of binary one dimensional annular photonic crystal including temperature dependent constituents, *Phys. E*, 2020, **119**, 114020.

10 M. M. Abadla, H. A. Elsayed and A. Mehaney, Novel design for the temperature sensing using annular photonic crystals, *Silicon*, 2021, **13**(12), 4737–4745.

11 M. S. Chen, C. J. Wu and T. J. Yang, Wave properties of an annular periodic multilayer structure containing the single-negative materials, *Phys. Lett.*, 2009, **373**(39), 3594–3600.

12 E. Udd, An overview of fiber-optic sensors, *Rev. Sci. Instrum.*, 1995, **66**(8), 4015–4030.

13 I. W. Jung, B. Park, J. Provine, R. T. Howe and O. Solgaard, Highly sensitive monolithic silicon photonic crystal fiber tip sensor for simultaneous measurement of refractive index and temperature, *J. Light: Technol.*, 2011, **29**(9), 1367–1374.

14 F. Fan, S. J. Chang, W. H. Gu, X. H. Wang and A. Q. Chen, Magnetically tunable terahertz isolator based on structured semiconductor magneto plasmonics, *IEEE Photonics Technol. Lett.*, 2012, **24**(22), 2080–2083.

15 A. G. Ardakani, Tunability of absorption with temperature in the terahertz regime based on photonic crystals containing graphene and defect insb layers, *Eur. Phys. J. B*, 2015, **88**, 1–8.

16 S. Chen, F. Fan, X. Wang, P. Wu, H. Zhang and S. Chang, Terahertz isolator based on nonreciprocal magneto-metasurface, *Opt. Express*, 2015, **23**(2), 1015.

17 A. Rashidi, C. Nayak, C. G. Bezerra, C. H. Costa and F. A. Pinheiro, Tunable terahertz absorption in Si/SiO_2-graphene multilayers: disorder and magneto-optical effects, *Appl. Opt.*, 2020, **59**(35), 11034–11040.

18 L. Xia, X. Zhang and D. Wang, Terahertz surface magneto-plasmons modulation with magnetized InSb hole array sheet, *Opt. Commun.*, 2019, **446**, 84–87.

19 B. Wan, H. Zhang and P. Wang, Nonreciprocal absorber with a narrow band of angular polarization sensitive regions based on a quasi-periodic structure, *Opt. Lett.*, 2021, **46**(8), 1934–1937.

20 F. Fan, S. J. Chang, W. H. Gu, X. H. Wang and A. Q. Chen, Magnetically tunable terahertz isolator based on structured semiconductor magneto plasmonics, *IEEE Photonics Technol. Lett.*, 2012, **24**(22), 2080–2083.

21 J. Sui, R. Dong, S. Liao, Z. Zhao, Y. Wang and H. F. Zhang, Janus Metastructure Based on Magnetized Plasma Material with and Logic Gate and Multiple Physical Quantity Detection, *Ann. Phys.*, 2023, **535**(3), 2200509.

22 S. S. Rao, J. T. Zhang and H. F. Zhang, A multifunctional and multiscale device of magnetic-controlled AND logical operation and detection based on the nonreciprocity of the magnetized InSb photonic structure, *Results Phys.*, 2021, **31**, 105058.

23 Z. Zang, Numerical analysis of optical bistability based on fiber Bragg grating cavity containing a high nonlinearity doped-fiber, *Opt. Commun.*, 2012, **285**(5), 521–526.

24 P. Rani, Y. Kalra and R. K. Sinha, Realization of AND gate in Y shaped photonic crystal waveguide, *Opt. Commun.*, 2013, **298**, 227–231.

25 Y. Ishizaka, Y. Kawaguchi, K. Saitoh and M. Koshiba, Design of ultra compact all-optical XOR and AND logic gates with low power consumption, *Opt. Commun.*, 2011, **284**(14), 3528–3533.

26 S. K. Tripathy, S. Sahu, C. Mohapatro and S. P. Dash, Implementation of optical logic gates using closed packed 2D-photonic crystal structure, *Opt. Commun.*, 2012, **285**(13–14), 3234–3237.

27 T. K. Liang, L. R. Nunes, M. Tsuchiya, K. S. Abedin, T. Miyazaki, D. Van Thourhout and H. K. Tsang, High speed logic gate using two-photon absorption in silicon waveguides, *Opt. Commun.*, 2006, **265**(1), 171–174.

28 Y. Yang, F. Yang, H. Wang, W. Yang and W. Jin, Temperature-insensitive hydrogen sensor with polarization-maintaining photonic crystal fiber-based Sagnac interferometer, *J. Light: Technol.*, 2015, **33**(12), 2566–2571.

29 M. Sovizi and M. Aliannezhadi, Localized surface plasmon resonance (LSPR) of coupled metal nanospheres in longitudinal, transverse and three-dimensional coupling configurations, *Optik*, 2022, **252**, 168518.

30 Y. Zhao, Y. N. Zhang, R. Q. Lv and J. Li, Electric field sensor based on photonic crystal cavity with liquid crystal infiltration, *J. Light: Technol.*, 2017, **35**(16), 3440–3446.

31 Y. Liu, S. Li, H. Chen, J. Li and W. Zhang, Surface plasmon resonance-induced high sensitivity refractive index sensor with adjustable measurement range based on an evanescent field-enhanced D-shaped five-hole photonic crystal fiber, *J. Phys. D*, 2020, **53**(11), 115107.

32 L. Lewin, The electrical constants of a material loaded with spherical particles, *J. Electron. Eng. Technol.*, 1947, **94**(27), 65–68.

33 X. Liu, C. Lan and K. Bi, Dual band metamaterial perfect absorber based on Mie resonances, *Appl. Phys. Lett.*, 2016, **109**(6), 062902.

34 L. Xuan, X. Kong and J. Wu, A smoothly-connected crescent transverse gradient coil design for 50 mT MRI system, *Appl. Magn. Reson.*, 2021, **52**(6), 649–660.

35 C. A. Hu, C. J. Wu, T. J. Yang and S. L. Yang, Analysis of optical properties in cylindrical dielectric photonic crystal, *Opt. Commun.*, 2013, **291**, 424–434.

36 M. S. Chen, C. J. Wu and T. J. Yang, Optical properties of a superconducting annular periodic multilayer structure, *Solid State Commun.*, 2009, **149**(43–44), 1888–1893.

37 S. K. Srivastava and A. Aghajamali, Investigation of reflectance properties in 1D ternary annular photonic crystal

containing semiconductor and high-T c superconductor, *J. Supercond. Novel Magn.*, 2016, **29**, 1423–1431.

38 Z. A. Zaky, A. M. Ahmed, A. S. Shalaby and A. H. Aly, Refractive index gas sensor based on the Tamm state in a one-dimensional photonic crystal: Theoretical optimisation, *Sci. Rep.*, 2020, **10**(1), 9736.

39 J. Homola, Surface plasmon resonance sensors for detection of chemical and biological species, *Chem. Rev.*, 2008, **108**(2), 462–493.

40 U. E. Spichiger-Keller, *Chemical sensors and biosensors for medical and biological applications*, 2008.

41 S. E. L. Ç. U. K. Atalay, A. O. Kaya, V. S. Kolat, H. Ü. S. E. Y. İ. N. Gencer and T. E. K. İ. N. Izgi, One-dimensional magnonic crystal for magnetic field sensing, *J. Supercond. Novel Magn.*, 2015, **28**, 2071–2075.

42 S. Ghorbani, M. Sadeghi and Z. Adelpour, A highly sensitive and compact plasmonic ring nano-biosensor for monitoring glucose concentration, *Laser Phys.*, 2019, **30**(2), 026204.

43 A. P. Kabilan, X. S. Christina and P. E. Caroline, Photonic crystal based all optical or and xo logic gates, *2010 Second International Conference on Computing, Communication and Networking Technologies*, IEEE, 2010, pp. 1–4.

44 Y. Zhang, L. Wang, P. Jia, C. Zhai, G. An, L. Liu and J. Su, High-sensitivity refractive index sensor with cascaded dual-core photonic crystal fiber based on vernier effect, *Optik*, 2022, **256**, 168488.

45 M. Pirzadi, A. Mir and D. Bodaghi, Realization of ultra-accurate and compact all-optical photonic crystal OR logic gate, *IEEE Photonics Technol. Lett.*, 2016, **28**(21), 2387–2390.

46 Y. Chen, J. Dong, T. Liu, Q. Zhu and W. Chen, Refractive index sensing performance analysis of photonic crystal containing graphene based on optical Tamm state, *Mod. Phys. Lett. B*, 2016, **30**(04), 1650030.

47 S. M. K. Alawsi and M. A. Jabbar, Refractive index and temperature sensor using HC-1550 infiltrating by different liquid crystal, *Opt. Photonics J.*, 2018, **8**(3), 29–39.